Journal of Materials Chemistry A

PAPER

View Article Online
View Journal

Cite this: DOI: 10.1039/c6ta01111j

High-performance $NaFePO_4$ formed by aqueous ion-exchange and its mechanism for advanced sodium ion batteries†

Wei Tang,‡[afg] Xiaohe Song,‡[b] Yonghua Du,‡[c] Chengxin Peng,[ag] Ming Lin,[d] Shibo Xi,[c] Bingbing Tian,[ag] Jiaxin Zheng,[b] Yuping Wu,[e] Feng Pan*[b] and Kian Ping Loh*[ag]

Received 4th February 2016
Accepted 1st March 2016

DOI: 10.1039/c6ta01111j

www.rsc.org/MaterialsA

Room-temperature sodium ion batteries (SIBs) have attracted tremendous attention recently as cheaper alternatives to lithium ion batteries (LIBs) for potential application in large-scale electrical energy storage stations. Among the various classes of iron phosphate cathodes used in SIBs, olivine $NaFePO_4$ is one of the most attractive host materials for advanced sodium ion batteries owing to its electrochemical profile and high theoretical capacity. As an alternative to the organic-based electrochemical ion-exchange process which is disadvantaged by sluggish dynamics and co-intercalation of Li^+, we investigated an aqueous-based, electrochemical-driven ion-exchange process to transform olivine $LiFePO_4$ into highly pure olivine $NaFePO_4$, which shows superior electrochemical performance. Using a combination of *ab initio* calculations and experiments, we demonstrate that the mechanism is attributed to the much faster Na^+/Li^+ ion-exchange kinetics of $NaFePO_4$ at the aqueous electrolyte/cathode interface compared to the organic electrolytes. Operando Fe K-edge XANES and XRD were also carried out to study the staged evolution of phases during the sodiation/desodiation of $NaFePO_4$ nanograins.

1 Introduction

Large scale electrical energy storage (EES) is increasingly considered for integration with renewable systems like solar and wind power to increase the availability and value of these resources.[1–11] The current generation of Li-ion batteries use oxides (such as $LiCoO_2$ and $LiMn_2O_4$) and olivine $LiFePO_4$ as cathodes, which creates a strong demand for Li worldwide, driving its price increase and potential geopolitical tension. In this regard, room temperature sodium-ion batteries are seriously being considered as alternatives to lithium-ion batteries due to the natural abundance and uniform geographic distribution of sodium.[12–25] Recently, several types of insertion material have been implemented as cathode materials in sodium- ion batteries. They can be classified as layered transition metal (TM) oxides,[18,26–32] tunnel-type oxides,[33–36] phosphates,[37–48] fluorides[49,50] and organic components.[51–55] Among them, iron-based phosphates have attracted the most attention because of the abundant and eco-friendly properties of Fe, as well as its ability to form compounds with Na.[56]

Yamada *et al.*, Nazar *et al.*, Chio *et al.* and Kang *et al.* have investigated the sodium electrochemistry of iron-based phosphates independently, such as $Na_2FeP_2O_7$,[57] Na_2FePO_4F,[42] $Na_4Fe_3(PO_4)_2(P_2O_7)$[58] and $NaFePO_4$.[56] Among the reported iron-based phosphates, olivine $NaFePO_4$ possesses the highest theoretical capacity (154 mA h g^{-1}) because of its light framework.[56,59] However, olivine $NaFePO_4$ is not the thermodynamically stable phase and cannot be obtained using traditional solid-state synthesis, whereas the thermodynamically favored maricite phase has a close framework which disallows Na ion diffusion.[60,61] Using an ion exchange method, olivine phase $NaFePO_4$ was typically synthesized *via* organic-based electrochemical insertion of sodium ions into chemically or electrochemically delithiated $FePO_4$.[39,41,43,62–64] This process is usually performed through a two-step procedure, involving firstly the delithiation of $LiFePO_4$ in an organic lithium cell by organic chemical oxidation, and secondly the use of the delithiated electrode ($FePO_4$) in a new cell, where lithium was replaced by

[a]Department of Chemistry, National University of Singapore, 3 Science Drive 3, Singapore 117543. E-mail: chmlohkp@nus.edu.sg

[b]School of Advanced Materials, Peking University Shenzhen Graduate School, Shenzhen, 518055, China. E-mail: panfeng@pkusz.edu.cn

[c]Institute of Chemical and Engineering Sciences, A*STAR, 1 Pesek Road, Jurong Island, 627833, Singapore

[d]Institute of Materials Research and Engineering, A*STAR, 2 Fusionopolis Way, #08-03 Innovis, Singapore 138634

[e]New Energy and Materials Laboratory (NEML), Department of Chemistry & Shanghai Key Laboratory of Molecular Catalysis and Innovative Materials, Fudan University, Shanghai, 200433, China

[f]NUS Graduate School for Integrative Sciences and Engineering, 28 Medical Drive #05-01, Singapore 117597

[g]Centre for Advanced 2D Materials and Graphene Research Centre, National University of Singapore, 6 Science Drive 2, Singapore 117546

† Electronic supplementary information (ESI) available: Detailed ion-exchange process, electrochemical performance, *in situ* XANES and calculation method have been provided. See DOI: 10.1039/c6ta01111j

‡ These authors contributed equally.

sodium metal as the anode. The phase evolution of electrochemically synthesized Na_xFePO_4 during sodiation/desodiation has been studied by Yamada *et al.*,[62] Casas-Cabanas *et al.*[43,63] and Moreau *et al.*[41,65] One observation is that the charge/discharge behavior of $NaFePO_4$ is asymmetric, which is manifested by a two-plateau charging plot. It was inferred that the desodiation process of $NaFePO_4$ involved the sequential transition between a solid–solid reaction and a biphasic reaction, through an intermediate $Na_{2/3}FePO_4$ phase. Casas-Cabanas *et al.* found the simultaneous existence of three phases: $FePO_4$, $Na_{2/3}FePO_4$, and $NaFePO_4$ during discharge.[43,63] However, previously reported olivine $NaFePO_4$ only has a capacity less than 100–120 mA h g^{-1} (theoretical value 154 mA h g^{-1}), which degrades after 100 cycles.[66] Despite the restricted performance, the limited purity of $NaFePO_4$ may hinder the further study of its sodiation/desodiation behavior. To date, the reasons for this remain unclear. Furthermore, for safe operation, it is necessary to avoid the use of sodium metal in the ion-exchange process.[60] Amorphous $NaFePO_4$ was also prepared to avoid the direct synthesis of olivine $NaFePO_4$. With a sloping charge/discharge plot, amorphous $NaFePO_4$ exhibited exceptional performance with ultrastable capacity up to 150 mA h g^{-1} in the potential range of 1.5–4 V.[67]

Aqueous electrolytes have been considered as potential alternatives to organic-based electrolytes regarding safety and cost. Feasible lithium and sodium electrochemistry in aqueous electrolytes has been previously reported.[48,68–73] Despite the improved electrochemical performance obtained compared to the organic-based systems in terms of rate capability and cyclability, of particular significance is the theoretical understanding of different Na^+/Li^+-based electrode process kinetics in aqueous and organic electrolytes and the electrolyte/cathode interface during the process remains unknown, which may hinder the further optimization of the aqueous electrolyte-based energy storage systems of lithium and sodium ions.

Herein, we investigate an aqueous-based electrochemically driven ion-exchange process to transform olivine $LiFePO_4$ into highly pure olivine $NaFePO_4$. Besides the advantage of not generating dangerous byproducts, improved electrochemical performance was obtained compared to the organic-based exchange systems (142 mA h g^{-1} at 0.1C, up to 6000 cycles at 10C). This should be attributed to the complete substitution of Li^+ by Na^+ in $NaFePO_4$, which ensures unrestricted one-dimensional (1D) channels for Na^+ insertion/extraction. Furthermore, a theoretical study of the Na^+/Li^+ migration process in the aqueous and organic electrolytes and the electrolyte/cathode interface was carried out to understand the origins of the superior ion-exchange in aqueous electrolyte. To understand the staging phenomena when the host material buffers mechanical strain, the sodium insertion/extraction mechanism in olivine $NaFePO_4$ synthesized by this method was also investigated by operando Fe K-edge X-ray absorption near edge structure (XANES) studies. Together with XRD studies, biphasic separation of $NaFePO_4$ and $Na_{2/3}FePO_4$ during the equilibrium stage upon sodiation was observed.

2 Experimental section

Details on the aqueous/organic ion exchange, calculation method, electrochemical characterisation, XRD, TEM and *in situ* XANES studies are provided in the ESI.†

The Fe K-edge XAFS experiment was performed at XAFCA beamline (*J. Synchrotron Radiat.*, 2015, **22**, 839), Singapore Synchrotron Light Source (SSLS). The electron storage ring of SSLS is operated with an energy of 0.7 GeV with normally a current of 200–300 mA. Transmission mode was applied. The $Na/NaFePO_4$ coin cells with holes ($D = 5$ mm) at the centre were assembled for the operando XAFS study. The holes were sealed using Kapton tapes, which allowed the X-rays through but prevented air from entering the cell. In particular, a 50 nm Al thin film was coated on the sealed Kapton tapes by a thermal evaporator since sodium is much more sensitive to moisture/air than lithium. The thickness of the Al film was optimized to get the best results (**Caution**! Without the Al coating layer, the *in situ* cell will degrade quickly in testing). To avoid the significant absorption of X-rays by glass fibers, a Waterman filter paper was used as the separator in the $Na/NaFePO_4$ cell. The operando X-ray absorption near edge structure (XANES) study was performed at the Fe K-edge to monitor the change of the valence state of the Fe in the cathode material. XANES and extended X-ray absorption fine structure (EXAFS) data reduction followed standard methods using the ATHENA software package (*J. Synchrotron Radiat.*, 2005, **12**, 537).

3 Results and discussion

The electrochemically driven aqueous ion-exchanging of commercial olivine $LiFePO_4$ into $NaFePO_4$ was carried out in a three-electrode electrochemical system with a SCE (saturated calomel electrode) and a platinum electrode as the reference and counter electrode, respectively. Firstly, the $LiFePO_4$ electrode was galvanostatically delithiated to become $FePO_4$ in aqueous Li_2SO_4 electrolyte; then the same electrode ($FePO_4$) was galvanostatically sodiated to become $NaFePO_4$ in aqueous Na_2SO_4 electrolyte, and directly used as the cathode in SIBs after drying. Since anions are very crucial for temporary compensation of the excess positive electrode charge during the intercalation/deintercalation process, herein SO_4^{2-} anions are selected as the electrolyte anions which can provide the fastest intercalation/deintercalation kinetics.[72] This open-air ion-exchange unit is easy to operate and sustainable since there is no requirement for an inert atmosphere and no consumption of organic solvent or lithium metal, whereas all these are required in the organic ion-exchange system. The lithium ions which have accumulated in the electrolyte following the delithiation process can be easily recycled for other applications (inductively coupled plasma (ICP) results demonstrating the accumulation of Li^+ are shown in Fig. S1†).

Fig. 1a shows the voltage profile of delithiation of olivine $LiFePO_4$, evolving on the expected 0.45 V (*vs.* SHE) plateau and delivering a capacity close to the theoretical value of 170 mA h g^{-1} even at 2.5C (around 0.4 h). Subsequently, the capacity of 151 mA h g^{-1} (based on $NaFePO_4$) was delivered upon sodiation

at 0.5C (around 2 h), which is also close to the theoretical capacity of $NaFePO_4$. Both results demonstrate that the ion-exchange process, which occurs at 10 times higher rate than the organic-based ion exchange process, was completed in aqueous electrolyte.[64]

As shown in Fig. S2,† the morphology of $NaFePO_4$ was preserved very well after the aqueous-based ion-exchange. EDX mapping also indicates a uniform distribution of sodium in the whole electrode. TEM (Fig. 1b) and STEM (Fig. 1c) show that $NaFePO_4$ preserves a "many-particle system" of 100–200 nm particles, which is similar to the morphology of pristine $LiFePO_4$ as shown in Fig. S3.† As shown in the HRTEM of $NaFePO_4$ (Fig. 1d), the (101) and (210) planes were clearly observed along the zone axis of (−121). Moreover the atomic arrangement revealed in the HRTEM image (inset in Fig. 1d) is identical to the simulated atomic configuration viewed along the (−121) orientation. The retention of crystal structure during the transformation from $LiFePO_4$ to $NaFePO_4$ can be explained by the strong P–O bonds in the olivine structure which can accommodate the change in ionic radius from Li^+ to Na^+.[74,75] We also noted that after ion exchange, there was no obvious electrochemical corrosion of aluminum foil within this operating potential (SEM images of aluminum foil before and after ion exchange are shown in Fig. S4†). The low concentration of Al^{3+} in the electrolyte can effectively suppress the possible intercalation of Al^{3+} into the oxide framework, as previously reported.[76]

XRD was used to follow the changes in crystalline phases during the ion-exchange process. Fig. 1e shows the XRD patterns of $LiFePO_4$, $FePO_4$ and $NaFePO_4$ in which no residual peaks of $LiFePO_4$ and $FePO_4$ were identified in the synthesized $NaFePO_4$, indicating that $LiFePO_4$ (olivine, JSPDS no. 83-2092) had been delithiated completely to form pure olivine $FePO_4$ (heterosite JCPDS card no. 42-0579); and $FePO_4$ was further sodiated to transform into pure olivine $NaFePO_4$. The Fe K-edge XANES of $LiFePO_4$, $FePO_4$ and $NaFePO_4$ in Fig. 1f show that the Fe valence in $NaFePO_4$ and $LiFePO_4$ is almost the same; we can conclude that the olivine $LiFePO_4$ has been completely transformed into olivine $NaFePO_4$ by the aqueous ion-exchange process. The lattice parameters were determined by XRD Rietveld refinement, as summarized in Fig. S5 and Table S1.†

For comparison, $NaFePO_4$ was also prepared following the conventional organic ion-exchange process under different conditions. XRD and ICP were used to determine the phase purity of as-prepared samples. In contrast to the aqueous ion-exchange process, unsodiated $FePO_4$ and Li_xFePO_4 impurities were detected in the as-prepared $NaFePO_4$ by organic ion exchange (Fig. S6†). ICP test was applied, and the data shown in Table 1 demonstrate that there are residual Li ions adsorbed on the $FePO_4$ electrodes delithiated in both organic and aqueous electrolytes. As shown in Table 1, the residual Li^+ in $FePO_4$ delithiated in organic electrolyte shown in ICP analysis could be attributed to two sources: (1) un-delithiated $LiFePO_4$ due to reaction dynamics (see Fig. S6(i)† for the obvious residual $LiFePO_4$ peaks in XRD pattern when delithiated at 2.5C), (2) Li^+ adsorbed on the surface of materials. By applying a slower delithiation rate (1C and 0.1C) and constant voltage charge (0.1C, voltage charge until 0.01C), the un-delithiated contribution should be negligible, while the residual Li^+ may mainly result from surface adsorption. The surface Li^+ residual indicated by ICP is around 0.19/$FePO_4$. Cathode electrolyte interphase (CEI)

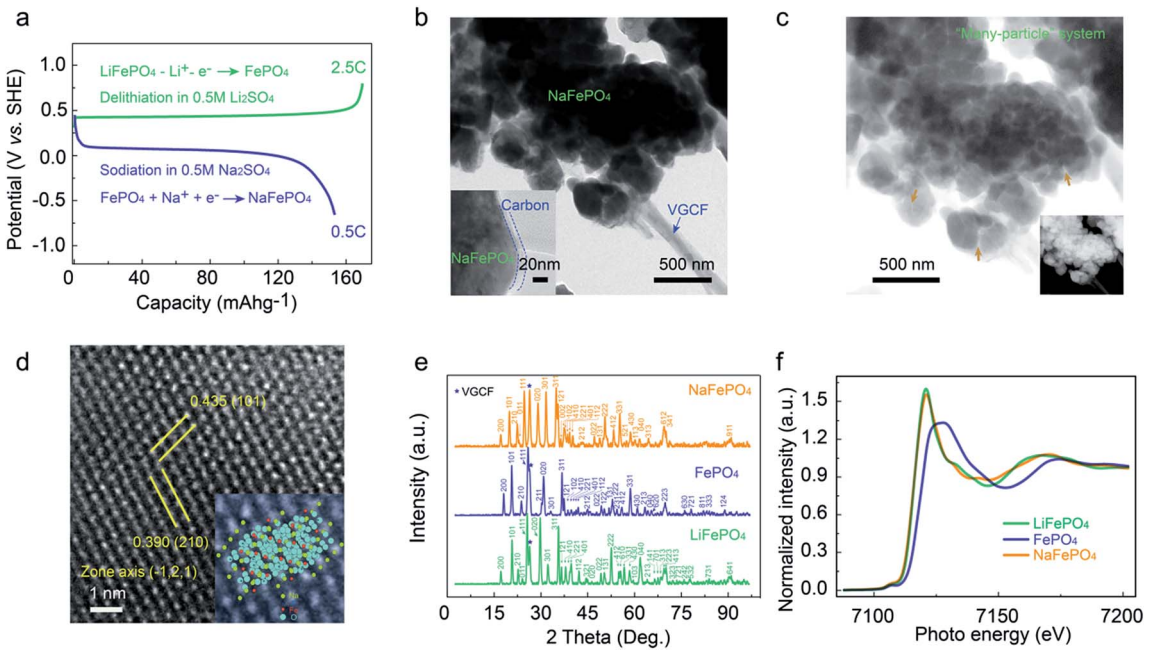

Fig. 1 (a) Delithiation and sodiation plot in aqueous electrolytes; (b) TEM, (c) inverted STEM and (d) HRTEM images of as-prepared $NaFePO_4$ by aqueous ion-exchange; (e) XRD patterns and (f) XANES spectra of pristine $LiFePO_4$, as-prepared $FePO_4$ and $NaFePO_4$. Inset in (b) shows an intact carbon layer on $NaFePO_4$ inherited from pristine $LiFePO_4$; inset in (c) shows the original STEM image; inset in (d) shows the simulated atomic configurations of $NaFePO_4$ viewed from zone (−121) match well with the obtained TEM image.

Table 1 ICP analysis of delithiated $FePO_4$ electrodes and as-prepared $NaFePO_4$ electrodes in different electrolytes

Organic electrolyte		Aqueous electrolyte	
2.5C delithiated $FePO_4$	$Li_{0.502}FePO_4$	2.5C delithiated $FePO_4$	$Li_{0.191}FePO_4$
1C delithiated $FePO_4$	$Li_{0.198}FePO_4$	1C delithiated $FePO_4$	$Li_{0.185}FePO_4$
0.1C delithiated $FePO_4$ with equilibrium	$Li_{0.190}FePO_4$	0.5C sodiation with 2.5C delithiated electrode	$Na_{0.937}Li_{0.05}FePO_4$
0.1C sodiation with 0.1C delithiated electrode	$Na_{0.610}Li_{0.173}FePO_4$		

films composed of organic byproducts such as Li_2CO_3, LiOH and LiF may partially contribute to the detected residual Li^+.[77–79] However, taking the low operating potential/temperature applied in this work and the existence of vinylene carbonate in the electrolyte, the CEI formed at the electrode surface during charging in the organic electrolyte system could be effectively supressed.[78,79] Upon sodiation, the adsorbed Li^+ may co-intercalate into the $FePO_4$ host, inducing the impurity $NaFePO_4$ as shown in the XRD pattern (Fig. S6(iv) and (v)†). The ICP determination is consistent with the XRD result while the composition of the electrode 0.1C sodiated with 0.1C delithiated electrode was analysed to be $Na_{0.610}Li_{0.173}FePO_4$. A similar amount of Li^+ (0.18–0.19/$FePO_4$) was found to be adsorbed on the surface of $FePO_4$ electrodes delithiated in aqueous electrolyte as shown in Table 1. However, the composition of electrode sodiated at 0.5C with washed 2.5C delithiated electrode using the aqueous ion-exchange process is determined to be $Na_{0.937}Li_{0.05}FePO_4$ (Table 1). It is obvious that much less residual Li remains and much more Na is sodiated in the aqueous ion-exchange process compared to the organic ion-exchange process, in good agreement with the previous XRD result where no residual Li_xFePO_4 and $FePO_4$ was detected in the aqueous-exchanged $NaFePO_4$.

Given all the results above, the main reasons for the impurity in $NaFePO_4$ obtained in the organic electrolyte are attributed to the sluggish sodium dynamics and co-insertion of residual lithium during the organic ion-exchange process. The advantage of high purity $NaFePO_4$ prepared by the aqueous method as compared to the organic method is significant, which can be assigned to the much less reintercalation of residual Li and faster sodiation dynamics during the aqueous ion-exchange process than the organic one. Further analysis is provided in the following section.

To understand the different intercalation kinetics in organic and aqueous electrolytes, an atomic level calculation and comparison of Na^+/Li^+ energies involved in the migration process in the electrolytes and the electrolyte/cathode interface is necessary. It is well known that upon dissolution of alkali salts, cations form "solvated ions" with solvent molecules.[80,81] In the organic case, we studied only EC (ethylene carbonate) despite the existence of DMC (dimethyl carbonate) in the practical electrolyte mixture, due to the fact that the ion solvation is dominated by EC.[82] Previous theoretical studies show that the hydrated M ion in aqueous solution and solvated M ion in EC-based electrolyte both have a two-shell structure (M = Li, Na).[81,83–85] The inner sphere is composed of four EC molecules forming $M^+(EC)_4$ or four H_2O molecules forming $M^+(H_2O)_4$ with coordination between the lone pair electrons of oxygen atoms and M ions (M–O), as shown in Fig. 2a and b. Note that, due to the larger radius of sodium, two extra H_2O molecules may coordinate with Na^+ to form $Na^+(H_2O)_6$ (Fig. S7†).[84] In view of the fact that the desolvation energy of the first two H_2O is quite small (see Table S2† for the desolvation energies), only the $Na^+(H_2O)_4$ complex is studied here. The outer shell is composed of several organic molecules or H_2O molecules weakly bonding with the inner sphere.[81,84]

The higher conductivity of ions in aqueous electrolytes compared to organic electrolytes (see Fig. S8† for the impedance study of $LiFePO_4$ in aqueous and organic electrolytes) allows the solvated ions to diffuse faster from the bulk electrolyte to the desolvation region near the surface of the electrode in aqueous electrolytes.[68–71] The transport process (including the desolvation and adsorption processes) at the solid/electrolyte interface was further studied to understand the fast dynamics of sodium ions in aqueous electrolytes (see ESI section 1† for a detailed description of the models and calculations). Fig. 2a and b show the possible behavior for Na/Li ion diffusion in close proximity to the solid/liquid (organic) interface (the desolvation layer and inner-Helmholtz layer). Our DFT study demonstrates that only one EC molecule can be adsorbed on a surface Na-site for $NaFePO_4$ and a surface Fe-site on the (010) surface of $FePO_4$, due to the steric hindrance as shown in Fig. 2b(iv) and (vi), while three H_2O and one H_2O molecules can be adsorbed on the surfaces of $NaFePO_4$ and $FePO_4$, respectively (Fig. 2a(iii) and (iv)), due to the smaller size of H_2O molecule (detailed *ab initio* calculated H_2O/EC absorption structures can be found in Fig. S9†). The surface adsorbed water can be easily removed after dried at 80 °C before battery fabrication. As shown in Fig. S10,† the TGA plot of $NaFePO_4$ after drying at 80 °C demonstrates no obvious water adsorption in the electrode. XPS also confirmed that there are no obvious changes in the O 1s signal before and after sodium exchange (Fig. S11†).[76] These structures are quite similar to our previous observations in $LiFePO_4$ and $FePO_4$.[80] To allow the intercalation of one Na^+ into $FePO_4$ to form a Na_xFePO_4 complex, only two H_2O molecules need to be stripped away from its primary solvation complex ($Na^+(H_2O)_4$) (Fig. 2a(i) and (ii)), followed by the approach of the resultant $Na^+(H_2O)_2$ to the surface of $FePO_4$ to form $NaFePO_4$ as shown in Fig. 2a(iv). However, in the case of an organic electrolyte, three EC molecules have to be stripped away from the primary solvation sphere ($Na^+(EC)_4$) before the resultant $Na^+(EC)$ complex can approach the concavities at the surface of $FePO_4$ (as shown in Fig. 2b(i)–(iii)). Moreover, the EC molecule adsorbed on the surface of $FePO_4$ needs to be stripped away before the adsorption of $Na^+(EC)$ due to the steric

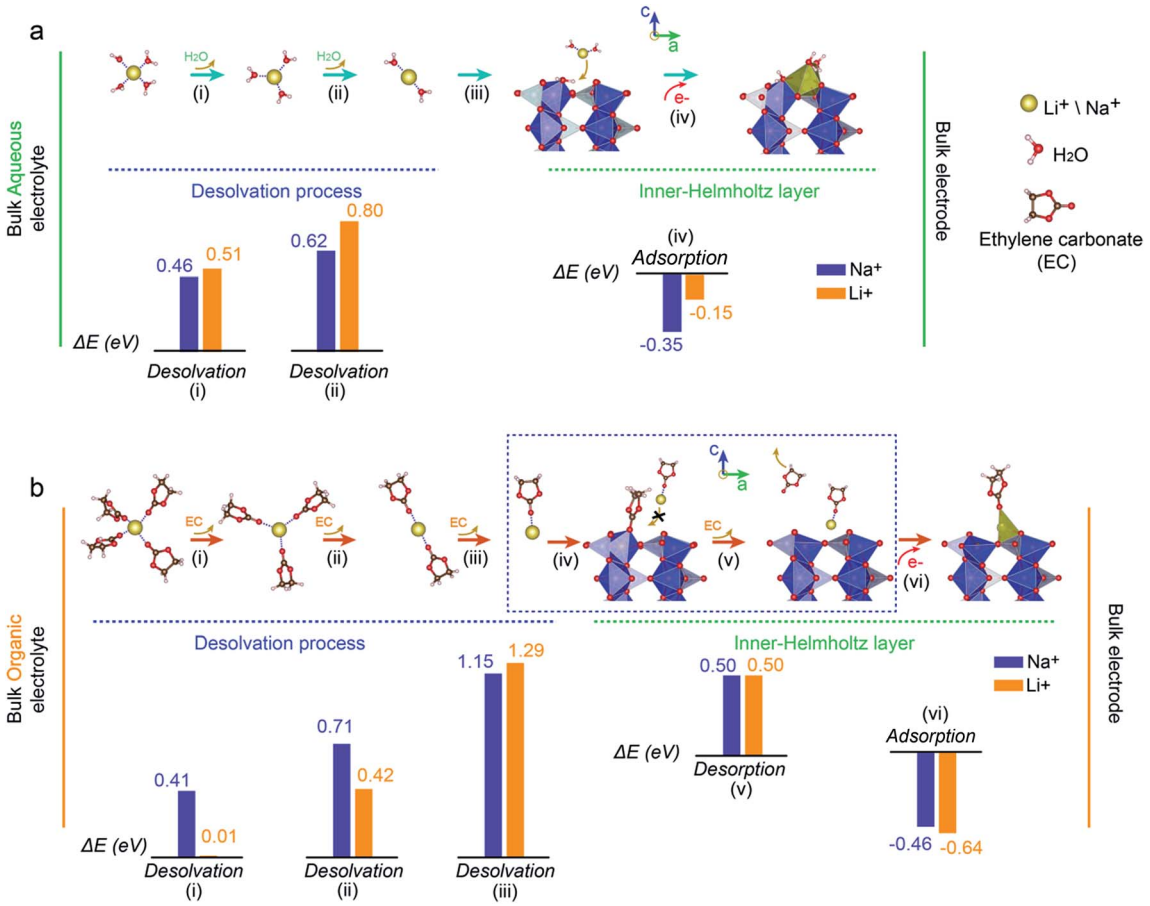

Fig. 2 The reaction profiles for Li/Na ion transport across the (a) $FePO_4/H_2O$ and (b) $FePO_4$/EC interfaces. The energies for each step during the desolvation process and adsorption process are plotted as bars accordingly (blue bars for sodium-based, orange bars for Li-based). The desolvation process is endothermic, while the adsorption process is exothermic.

hindrance (Fig. 2b(iv)–(vi)). Thus, although the initial desolvation energies of two electrolyte molecules for sodium ions in aqueous and organic electrolytes are quite similar (ΔE(i) and (ii) as indicated by blue bars), the additional desolvation processes (indicated by the blue dashed box in Fig. 2b) required in an organic electrolyte may increase the energy barriers for sodium intercalation, which are specifically calculated as ΔE(iii) = 1.15 eV and ΔE(v) = 0.5 eV (blue bars) in Fig. 2b, respectively.

It is also important to consider the ion-exchange process of Na and Li ions upon intercalation, as we found that there are Li ions adsorbed on the delithiated electrode in both electrolytes even after careful washing (Table 1). In the case of an aqueous system (Fig. 2a), the desolvation energy for $Na^+(H_2O)_n$ is lower than that for $Li^+(H_2O)_n$ in both steps (i) ($\Delta E(\mathrm{i})_{Na^+}$ = 0.46 eV, $\Delta E(\mathrm{i})_{Li^+}$ = 0.51 eV) and step (ii) ($\Delta E(\mathrm{ii})_{Na^+}$ = 0.62 eV, $\Delta E(\mathrm{i})_{Li^+}$ = 0.80 eV), indicating that the desolvation process of Na^+-solvated ion is easier than that of Li^+-solvated ion. In addition, the adsorption energy for Na^+ (ΔE(iv) = −0.35 eV) is much larger than Li^+ (ΔE(iv) = −0.15 eV). This means that surface adsorbed Li^+ will be easily substituted by Na^+ when delithiated $FePO_4$ is immersed into the sodium-based aqueous electrolyte, resulting in a pure sodium intercalation compound subsequently (the ICP results of the aqueous intercalated electrode in Table 1 only present a negligible lithium ion content).

In contrast, in the case of an organic-exchanged system (Fig. 2b), the desolvation energy for $Na^+(EC)_n$ is much higher than that for $Li^+(EC)_n$ in step (i) ($\Delta E(\mathrm{i})_{Na^+}$ = 0.41 eV, $\Delta E(\mathrm{i})_{Li^+}$ = 0.01 eV) and step (ii) ($\Delta E(\mathrm{ii})_{Na^+}$ = 0.71 eV, $\Delta E(\mathrm{i})_{Li^+}$ = 0.42 eV), meaning that Li^+ desolvation is easier in the first two steps. For step (iii), the desolvation energy for $Na^+(EC)_2$ is only slightly lower than $Li^+(EC)_2$. As a result, residual Li^+ will compete with Na^+ desolvation. In addition, the adsorption energy of Li^+ ($\Delta E(\mathrm{vi})_{Li^+}$ = −0.64 eV) is higher compared to that of Na^+ ($\Delta E(\mathrm{vi})_{Na^+}$ = −0.46 eV), indicating that Li^+ adsorption competes with Na^+. The competition between Li^+ and Na^+ upon desolvation and adsorption processes may induce the co-intercalation of Li^+ originating from the residual Li^+ of delithiated electrodes in the organic-exchanged system.

Based on these calculations, the competitive intercalation of Li^+ can be effectively suppressed in the aqueous ion-exchange process, while Li^+ will co-intercalate into $FePO_4$ in the organic ion-exchange process. Indeed, additional intercalation of lithium ions into as-prepared $FePO_4$ was previously observed without identification in an organic ion-exchange process,[64] which affects the purity of the final product and negatively affects the ultimate cycling capability.

The sodium storage performance of the aqueous-exchanged $NaFePO_4$ in organic media was characterized with coin cells in

half-cell configuration with sodium as the anode in the potential range of 2–4 V (*vs.* Na/Na^+). Fig. 3a shows reversible charge–discharge profiles of the $Na/NaFePO_4$ cells at 0.1C (1C = 154 mA h g^{-1}). In the first cycle, the specific charge and discharge capacities of the $NaFePO_4$ are 140 mA h g^{-1} and 142 mA h g^{-1}, respectively, corresponding to an initial coulombic efficiency close to 100%; and 92% capacity is retained for more than 200 cycles (Fig. 3c). The profiles for charge and discharge processes appear to be asymmetric. While a unique plateau can be identified during discharge, two continuous plateaus can be observed upon charge. This asymmetry is clearly observed in dQ/dV curves as shown in Fig. 3b. Only one sharp peak can be observed during sodiation whereas two oxidation peaks can be distinguished upon desodiation. These observations are consistent with previous reports on olivine $NaFePO_4$ prepared by organic ion exchange.[39,64] XANES was carried out later to provide insights into the sodiation/desodiation mechanism. We note that the sodiation peak in dQ/dV curves (Fig. 3b) is very sharp and delivers 85% capacity within a voltage window of 0.1 V upon discharge (Fig. 3a), which is comparable with $Na_3V_2(PO_4)_3$.[37,45] This feature should be attributed to the well retained crystalline structure of $NaFePO_4$ after aqueous ion exchange, which enables homogenous sodium insertion in a narrow voltage window. As the BET surface area and tap density of $NaFePO_4$ were found to be 9.3013 m^2 g^{-1} (Fig. S12†) and 0.891 g cm^{-3} respectively, there may be slightly pseudo-capacitance-type reaction during Na^+ storage with the existence of a carbon coating and pores on/between $NaFePO_4$ nanoparticles.[86] It is worth mentioning that maricite $NaFePO_4$ was recently reported to be activated at a very low rate (*i.e.* 0.05C) through a crystalline-to-amorphous phase transition, even though the loss of crystalline structure will result in a sloping charge/discharge plot and relatively lower rate capability.[56] As shown in Fig. 3d, when the current is increased, the capacity of $NaFePO_4$ decreases due to the increased polarization. However, capacities of 100 mA h g^{-1}, 60 mA h g^{-1} and 38 mA h g^{-1} can still be delivered at 1C, 10C and 20C, respectively (Fig. 3e). Although the performance is not comparable with the rate capability of $LiFePO_4$, it is acceptable for an energy storage device. As shown in Fig. 3f, a coin cell with a mass loading of $NaFePO_4$ around 5 mg was used to light a white LED.

Considering the large lattice mismatch between $NaFePO_4$ and $FePO_4$ (17.58% in volume) which may give rise to phase segregation,[43] the cycle stability of aqueous ion-exchanged $NaFePO_4$ is quite impressive. As shown in Fig. 4a, the capacity retention of $NaFePO_4$ was 86%, 90% and 89% cycled at 0.5C, 1C and 2C after 500 cycles, respectively (82% capacity retention after 1000 cycles at 0.5C as shown in Fig. S13†). Even when cycled at a very high rate of 10C (Fig. 4b), $NaFePO_4$ possesses 70% of its initial capacity after 6000 cycles. Such a good cycle stability should be attributed to the complete substitution of Li^+ by Na^+ in $NaFePO_4$, which ensures unrestricted one-dimensional (1D) channels for Na^+ insertion/extraction.[39] Furthermore the strong polyanion P–O bonds help to preserve the olivine structure during multiple Na^+ insertion/extraction processes in the host structure along the [010] direction.[61,64] For comparison, the electrochemical performance of Na_xFePO_4 ($0 < x < 1$) synthesized from organic ion exchange is shown in Fig. S14.† Apart from a much lower capacity due to incomplete ion exchange, the organic ion-exchanged $NaFePO_4$ shows an inferior cycle stability compared to the aqueous ion-exchanged process. Fig. 4c, which compares the XRD patterns of the aqueous-exchanged $NaFePO_4$ observed after different cycles, confirms the reversibility of $NaFePO_4$ as judged from the preservation of the pristine olivine structure after multiple cycling, with only minor broadening of the XRD peaks after 5000 cycles

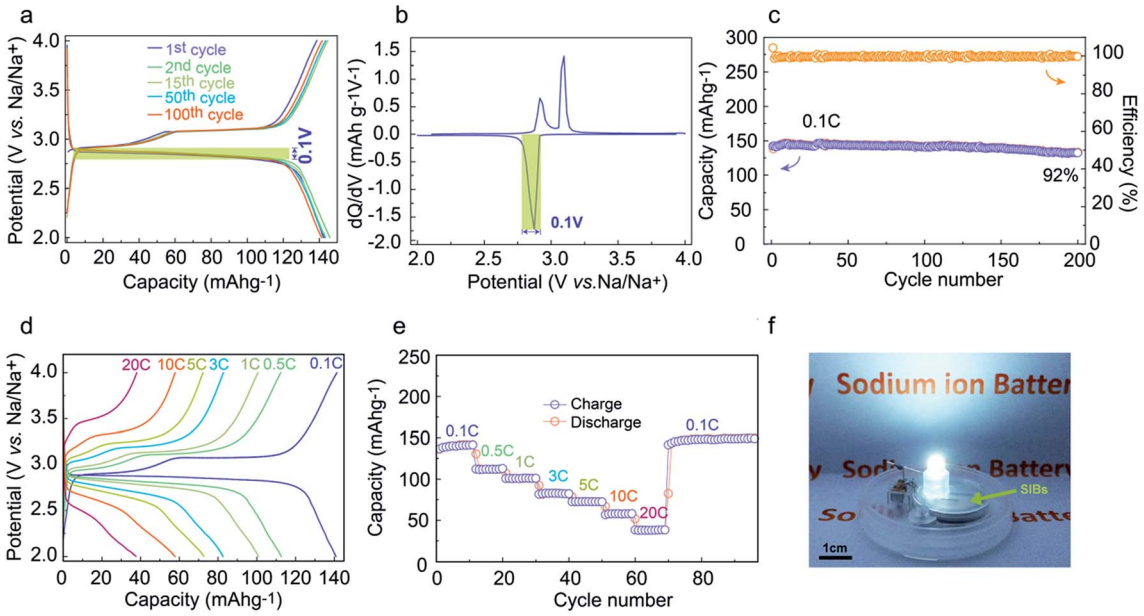

Fig. 3 Electrochemical performance of aqueous ion-exchanged $NaFePO_4$. (a) Charge and discharge plots, (b) dQ/dV curves and (c) cyclability at 0.1C. (d) Charge and discharge plots and (e) capacities at different rates up to 20C. (f) Photograph shows the lighting of one white LED powered by the aqueous ion-exchanged $NaFePO_4$ battery.

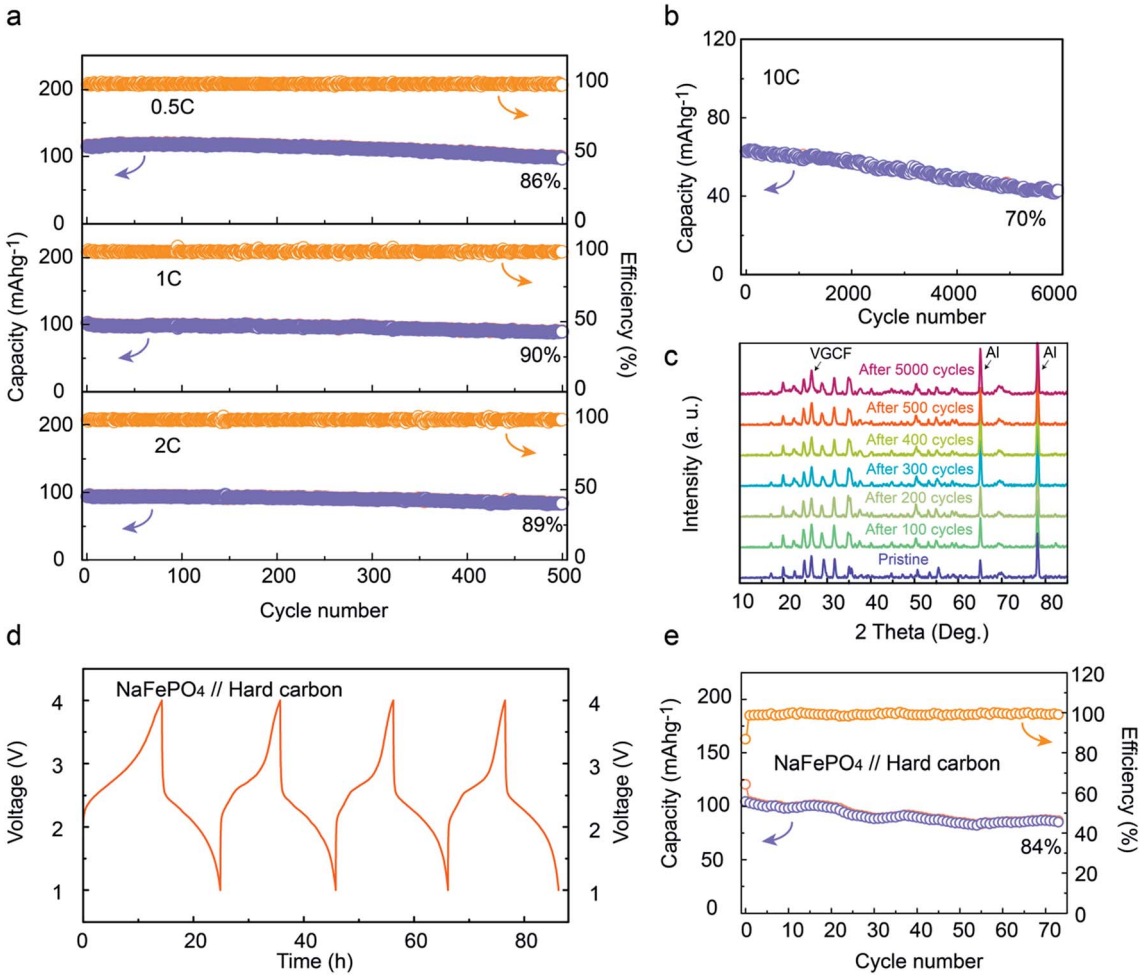

Fig. 4 Long-term cycle stability of aqueous ion-exchange $NaFePO_4$ at different rates: (a) 0.5C, 1C, 2C and (b) 10C. (c) XRD patterns of $NaFePO_4$ electrodes after different cycles to demonstrate the stability of $NaFePO_4$ during long-term cycling. (d) Charge and discharge plots at 0.1C and (e) cyclability at 1C for $NaFePO_4$//hard carbon full cells.

(TEM images of $NaFePO_4$ after 5000 cycles are shown in Fig. S15†).

To demonstrate the potential of aqueous ion-exchanged $NaFePO_4$ as a cathode in sodium ion batteries, a prototype full cell (coin cell) was fabricated by utilizing $NaFePO_4$ as a cathode and commercial hard carbon as the anode. The electrochemical performance of hard carbon is shown in Fig. S16.† Fig. 4d shows the charge/discharge curves of the full cell measured at 0.1C. The cell exhibits a voltage profile that mainly reflects the potential of $NaFePO_4$ and a capacity of around 140 mA h g^{-1}. Both the cycle stability and efficiency of the full cell are good. As shown in Fig. 4e, the full cell can deliver a capacity of 86 mA h g^{-1} after 60 cycles at 1C (84% capacity retention).

Synchrotron radiation based X-ray absorption spectroscopy (XAS) is a well-established method to determine the local atomic and electronic structure of the element of interest in a complex system. Operando XANES probes the oxidation states of the elements present in the battery system.[33,87–94] In the case of olivine Na_xFePO_4 ($0 < x < 1$), it has been reported by Lu and Yamada that its phase diagram is different from that of Li_x-$FePO_4$ due to the larger solubility limit of (sodium) vacancies, giving rise to a solid solution for x between 2/3 to 1, and a phase separated $FePO_4$ and Na_xFePO_4 at $0 < x < 2/3$.[62] XRD spectra collected at different equilibrium stages at 0.1C are shown in Fig. 5e and f (patterns 1–10), where the phase transition behavior agrees well with that of organic-exchanged olivine Na_xFePO_4 reported by Lu and Yamada. For example, a solid solution exists between the transition of $NaFePO_4$ (pattern 1) and $Na_{2/3}FePO_4$ (pattern 5). Above a critical phase of $Na_{2/3}FePO_4$, we can see the mixture of two sets of XRD patterns due to phase segregated $Na_{2/3}FePO_4$ and $FePO_4$ (pattern 6).

To obtain further insights into the dynamics of the sodiation/desodiation process, operando Fe K-edge XANES characterization of the $NaFePO_4$ during the initial galvanostatic cycling was carried out. Stacked plots and two-dimensional (2D) contour plots of operando XANES spectra for $NaFePO_4$ are shown in Fig. 5b and c, respectively. The voltage profile of the initial cycle is indicated in Fig. 5a alongside the XANES spectra. Upon desodiation, the Fe K-edge is rigidly shifted toward the higher binding energy, corresponding to increased Fe oxidation state during the charging process. Upon insertion of sodium ions, the oxidation state of Fe is reduced to its original state. To

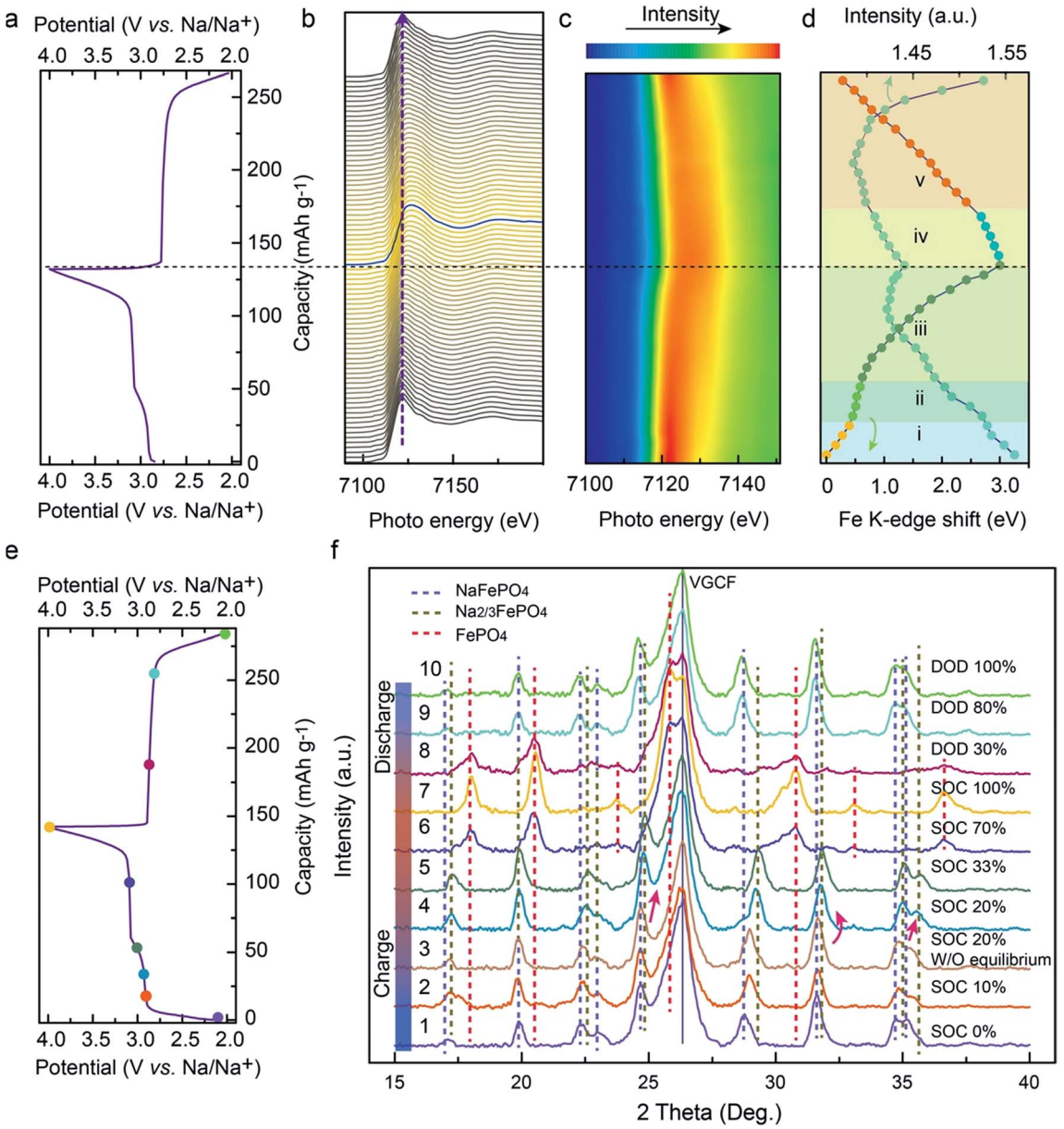

Fig. 5 *In situ* synchrotron Fe K-edge XANES and *ex situ* XRD studies of the aqueous ion-exchanged $NaFePO_4$ during initial cycles. (a) Voltage profile of the $NaFePO_4$ at the first cycle; (b) stacking plots, (c) two-dimensional (2D) contour plots and (d) the evolution of the Fe-edge energy (half weight) of operando XANES spectra of the $NaFePO_4$ at the first cycle. (e) Voltage profile of the $NaFePO_4$ at the second cycle. (f) XRD patterns of $NaFePO_4$ electrodes at different stages (equilibrium and non-equilibrium).

semi-quantitatively determine the oxidation states of Fe, the evolution of the edge energy (half weight) of the XANES spectra is plotted in Fig. 5d by taking $LiFePO_4$ as ref. 90. The energy evolution consists of five regions with different linear slopes associated with the bonding strength of 1s electrons of iron in different structures.[95] Well correlated with the charge–discharge profile, the asymmetry of the charge and discharge processes is obvious in the evolution of the Fe K-edge energy. Correlating with the charge/discharge plot in Fig. 5a, regions (i) and (ii) correspond to transformation of $NaFePO_4$ to the $Na_{2/3}FePO_4$ intermediate phase through a solid solution process;[62,63,94,96] the intermediate phase is then further desodiated to $FePO_4$ according to a nearly linear evolution of Fe edge energy in region (iii).[65] The two-stage charge mechanism should be associated with an asymmetric volume change from $NaFePO_4$ to $Na_{2/3}FePO_4$ (3.62%) and from $Na_{2/3}FePO_4$ to $FePO_4$ (13.48%).[43] The evolution in the XRD peak profiles upon equilibrium is well correlated with the observations in the aforementioned *in situ* XANES. During the charge process, $NaFePO_4$ is completely converted to the intermediate phase $Na_{2/3}FePO_4$ (pattern 5) before it can be further desodiated to $FePO_4$ (upon equilibrium; pattern 7); during the discharge process, the $FePO_4$ is partially transformed to the intermediate phase $Na_{2/3}FePO_4$ (dominated at the early stage of discharge; pattern 8) while $NaFePO_4$ is

formed simultaneously until the end of discharge (dominated at the later stage of discharge; pattern 9). At the end of discharge, $NaFePO_4$ is recovered as shown in pattern 10, thus yielding the highly reversible capacity of $NaFePO_4$. Interestingly, different features are observed in the XRD patterns of electrodes with/without equilibrium (with/without constant potential charge process) at a state of charge (SOC) 20% (the slope region linking two plateaus on the charge plot; patterns 3 and 4). Without equilibrium at SOC 20% (pattern 3), the XRD pattern can be explained by the solid-solution phase of $Na_{1-y}FePO_4$ ($0 < y < 1/3$).[62] Different from the non-equilibrium situation, upon equilibrium, the relaxation between particles may be completed; and biphasic separation due to $NaFePO_4$ and $Na_{2/3}FePO_4$ (pattern 4) is observed.[97] This phenomenon demonstrates that depending on the morphology of the Na_x-$FePO_4$ particles, which includes for example the homogeneity of the dispersion or the abilities of these particles to make effective electrical contacts in the "many-particle" system,[97] the conversion of $NaFePO_4$ to $Na_{2/3}FePO_4$ at the first charge stage may not form a monotone solid solution and relaxation between particles may be required. A monotone solid solution will reduce the hysteresis originating from the relaxation process (miscibility gap between solid solution and biphasic reaction).[98,99] A possible strategy to obtain a monotone solid solution may involve controlling the nanocrystallinity and facets of crystals, which is work in progress.

4 Conclusions

In summary, highly pure olivine $NaFePO_4$ was prepared by a simple aqueous ion-exchange process. Our results show that aqueous ion-exchanged $NaFePO_4$ exhibits a high reversible capacity of 142 mA h g^{-1} (0.1C) as well as an impressive cycle stability (6000 cycles at 10C). A theoretical study of the energetics of the Na^+/Li^+ migration process in the electrolyte and the electrolyte/cathode interface reveals that the desolvation and adsorption processes of sodium ions in aqueous electrolyte enable a faster Na^+ intercalating dynamics than Li^+. At the same time, the co-intercalation of Li^+ in the delithiated $FePO_4$ host is suppressed, leading to a higher ion-exchange efficiency than the organic ion-exchange process. Operando XANES of Fe K-edge, accompanied by XRD studies, was used to monitor the asymmetric but highly reversible phasic evolution of the highly pure $NaFePO_4$. The results indicate that the relaxation of Na_xFePO_4 particles occurs during the solid-solution stage during desodiation, resulting in biphasic separation due to $NaFePO_4$ and $Na_{2/3}FePO_4$ upon equilibrium. Although several issues need to be addressed before the strategy can be implemented in large scale application, the present study points out important correlations between the interfacial phenomena and the electrochemical profile, which provide useful clues for improving sodium electrochemistry in aqueous and organic electrolytes.

Acknowledgements

The manuscript was written through contributions of all the authors. All authors have given approval for the final version of the manuscript. The authors wish to acknowledge support from MOE Tier II grant "Interface Engineering of Graphene Hybrids for Energy Conversion" Grant Number: R-143-000-488-112, Guangdong Innovation Team Project (No. 2013N080) and Shenzhen Science and Technology Research Grant (No. ZDSY2013033 1145131323, JCYJ20140903101617271, JCYJ20150324141711645), and National Natural Science Foundation of China (No. 21506126).

Notes and references

1 M. Armand and J. M. Tarascon, *Nature*, 2008, **451**, 652–657.
2 J. B. Goodenough, *Energy Environ. Sci.*, 2014, **7**, 14–18.
3 M. M. Thackeray, C. Wolverton and E. D. Isaacs, *Energy Environ. Sci.*, 2012, **5**, 7854–7863.
4 M.-C. Lin, M. Gong, B. Lu, Y. Wu, D.-Y. Wang, M. Guan, M. Angell, C. Chen, J. Yang, B.-J. Hwang and H. Dai, *Nature*, 2015, **520**, 324–328.
5 J. C. Bachman, R. Kavian, D. J. Graham, D. Y. Kim, S. Noda, D. G. Nocera, Y. Shao-Horn and S. W. Lee, *Nat. Commun.*, 2015, **6**, 7040.
6 N.-S. Choi, Z. Chen, S. A. Freunberger, X. Ji, Y.-K. Sun, K. Amine, G. Yushin, L. F. Nazar, J. Cho and P. G. Bruce, *Angew. Chem., Int. Ed.*, 2012, **51**, 9994–10024.
7 M. R. Lukatskaya, O. Mashtalir, C. E. Ren, Y. Dall'Agnese, P. Rozier, P. L. Taberna, M. Naguib, P. Simon, M. W. Barsoum and Y. Gogotsi, *Science*, 2013, **341**, 1502–1505.
8 D. Su, S. Dou and G. Wang, *Adv. Energy Mater.*, 2015, **5**, 1401205.
9 R. Hu, G. H. Waller, Y. Wang, Y. Chen, C. Yang, W. Zhou, M. Zhu and M. Liu, *Nano Energy*, 2015, **18**, 232–244.
10 D. Kong, C. Cheng, Y. Wang, J. I. Wong, Y. Yang and H. Y. Yang, *J. Mater. Chem. A*, 2015, **3**, 16150–16161.
11 L. Yu, Z. Wang, L. Zhang, H. B. Wu and X. W. Lou, *J. Mater. Chem. A*, 2013, **1**, 122–127.
12 M. D. Slater, D. Kim, E. Lee and C. S. Johnson, *Adv. Funct. Mater.*, 2013, **23**, 947–958.
13 V. Palomares, P. Serras, I. Villaluenga, K. B. Hueso, J. Carretero-Gonzalez and T. Rojo, *Energy Environ. Sci.*, 2012, **5**, 5884–5901.
14 H. Pan, Y.-S. Hu and L. Chen, *Energy Environ. Sci.*, 2013, **6**, 2338–2360.
15 S. P. Ong, V. L. Chevrier, G. Hautier, A. Jain, C. Moore, S. Kim, X. Ma and G. Ceder, *Energy Environ. Sci.*, 2011, **4**, 3680–3688.
16 P. Barpanda, G. Oyama, S.-i. Nishimura, S.-C. Chung and A. Yamada, *Nat. Commun.*, 2014, **5**, 4358.
17 Y. Shao, J. Xiao, W. Wang, M. Engelhard, X. Chen, Z. Nie, M. Gu, L. V. Saraf, G. Exarhos, J.-G. Zhang and J. Liu, *Nano Lett.*, 2013, **13**, 3909–3914.
18 N. Yabuuchi, M. Kajiyama, J. Iwatate, H. Nishikawa, S. Hitomi, R. Okuyama, R. Usui, Y. Yamada and S. Komaba, *Nat. Mater.*, 2012, **11**, 512–517.
19 M. Moradi, Z. Li, J. Qi, W. Xing, K. Xiang, Y.-M. Chiang and A. M. Belcher, *Nano Lett.*, 2015, **15**, 2917–2921.

20 W.-J. Li, S.-L. Chou, J.-Z. Wang, H.-K. Liu and S.-X. Dou, *Nano Lett.*, 2013, **13**, 5480–5484.
21 Y. Yan, Y.-X. Yin, Y.-G. Guo and L.-J. Wan, *Adv. Energy Mater.*, 2014, **4**, 1301584.
22 J.-Y. Liao and A. Manthiram, *Nano Energy*, 2015, **18**, 20–27.
23 D. Li, H. Chen, G. Liu, M. Wei, L.-x. Ding, S. Wang and H. Wang, *Carbon*, 2015, **94**, 888–894.
24 S. Wang, L. Xia, L. Yu, L. Zhang, H. Wang and X. W. Lou, *Adv. Energy Mater.*, 2015, DOI: 10.1002/aenm.201502217.
25 D. Li, L. Zhang, H. Chen, L.-x. Ding, S. Wang and H. Wang, *Chem. Commun.*, 2015, **51**, 16045–16048.
26 J.-Y. Hwang, S.-M. Oh, S.-T. Myung, K. Y. Chung, I. Belharouak and Y.-K. Sun, *Nat. Commun.*, 2015, **6**, 6865.
27 M. Guignard, C. Didier, J. Darriet, P. Bordet, E. Elkaïm and C. Delmas, *Nat. Mater.*, 2013, **12**, 74–80.
28 J. Billaud, R. J. Clément, A. R. Armstrong, J. Canales-Vázquez, P. Rozier, C. P. Grey and P. G. Bruce, *J. Am. Chem. Soc.*, 2014, **136**, 17243–17248.
29 H. Liu, J. Xu, C. Ma and Y. S. Meng, *Chem. Commun.*, 2015, **51**, 4693–4696.
30 S. Komaba, N. Yabuuchi, T. Nakayama, A. Ogata, T. Ishikawa and I. Nakai, *Inorg. Chem.*, 2012, **51**, 6211–6220.
31 D. Buchholz, A. Moretti, R. Kloepsch, S. Nowak, V. Siozios, M. Winter and S. Passerini, *Chem. Mater.*, 2013, **25**, 142–148.
32 S. Guo, P. Liu, Y. Sun, K. Zhu, J. Yi, M. Chen, M. Ishida and H. Zhou, *Angew. Chem., Int. Ed.*, 2015, **54**, 11701–11705.
33 Y. Wang, J. Liu, B. Lee, R. Qiao, Z. Yang, S. Xu, X. Yu, L. Gu, Y.-S. Hu, W. Yang, K. Kang, H. Li, X.-Q. Yang, L. Chen and X. Huang, *Nat. Commun.*, 2015, **6**, 6401.
34 M. M. Doeff, M. Y. Peng, Y. Ma and L. C. De Jonghe, *J. Electrochem. Soc.*, 1994, **141**, L145–L147.
35 Y. Cao, L. Xiao, W. Wang, D. Choi, Z. Nie, J. Yu, L. V. Saraf, Z. Yang and J. Liu, *Adv. Mater.*, 2011, **23**, 3155–3160.
36 F. Sauvage, L. Laffont, J. M. Tarascon and E. Baudrin, *Inorg. Chem.*, 2007, **46**, 3289–3294.
37 S. Li, Y. Dong, L. Xu, X. Xu, L. He and L. Mai, *Adv. Mater.*, 2014, **26**, 3545–3553.
38 Y.-U. Park, D.-H. Seo, H. Kim, J. Kim, S. Lee, B. Kim and K. Kang, *Adv. Funct. Mater.*, 2014, **24**, 4603–4614.
39 Y. Zhu, Y. Xu, Y. Liu, C. Luo and C. Wang, *Nanoscale*, 2013, **5**, 780–787.
40 K. Zaghib, J. Trottier, P. Hovington, F. Brochu, A. Guerfi, A. Mauger and C. M. Julien, *J. Power Sources*, 2011, **196**, 9612–9617.
41 P. Moreau, D. Guyomard, J. Gaubicher and F. Boucher, *Chem. Mater.*, 2010, **22**, 4126–4128.
42 B. L. Ellis, W. R. M. Makahnouk, Y. Makimura, K. Toghill and L. F. Nazar, *Nat. Mater.*, 2007, **6**, 749–753.
43 M. Casas-Cabanas, V. V. Roddatis, D. Saurel, P. Kubiak, J. Carretero-Gonzalez, V. Palomares, P. Serras and T. Rojo, *J. Mater. Chem.*, 2012, **22**, 17421–17423.
44 M. Peng, B. Li, H. Yan, D. Zhang, X. Wang, D. Xia and G. Guo, *Angew. Chem., Int. Ed.*, 2015, **54**, 6452–6456.
45 C. Zhu, K. Song, P. A. van Aken, J. Maier and Y. Yu, *Nano Lett.*, 2014, **14**, 2175–2180.
46 S.-Y. Chung, J. T. Bloking and Y.-M. Chiang, *Nat. Mater.*, 2002, **1**, 123–128.
47 J. Barker, M. Y. Saidi and J. L. Swoyer, *Electrochem. Solid-State Lett.*, 2003, **6**, A1–A4.
48 Y. Fang, Q. Liu, L. Xiao, X. Ai, H. Yang and Y. Cao, *ACS Appl. Mater. Interfaces*, 2015, **7**, 17977–17984.
49 J. Zhu and D. Deng, *Angew. Chem., Int. Ed.*, 2015, **54**, 3079–3083.
50 Y.-N. Zhou, M. Sina, N. Pereira, X. Yu, G. G. Amatucci, X.-Q. Yang, F. Cosandey and K.-W. Nam, *Adv. Funct. Mater.*, 2015, **25**, 696–703.
51 K. Sakaushi, E. Hosono, G. Nickerl, T. Gemming, H. Zhou, S. Kaskel and J. Eckert, *Nat. Commun.*, 2013, **4**, 1485.
52 L. Wang, J. Song, R. Qiao, L. A. Wray, M. A. Hossain, Y.-D. Chuang, W. Yang, Y. Lu, D. Evans, J.-J. Lee, S. Vail, X. Zhao, M. Nishijima, S. Kakimoto and J. B. Goodenough, *J. Am. Chem. Soc.*, 2015, **137**, 2548–2554.
53 S. Wang, L. Wang, Z. Zhu, Z. Hu, Q. Zhao and J. Chen, *Angew. Chem.*, 2014, **126**, 6002–6006.
54 P. Novák, K. Müller, K. S. V. Santhanam and O. Haas, *Chem. Rev.*, 1997, **97**, 207–282.
55 H.-G. Wang, S. Yuan, D.-L. Ma, X.-L. Huang, F.-L. Meng and X.-B. Zhang, *Adv. Energy Mater.*, 2014, **4**, 1301651.
56 J. Kim, D.-H. Seo, H. Kim, I. Park, J.-K. Yoo, S.-K. Jung, Y.-U. Park, W. A. Goddard Iii and K. Kang, *Energy Environ. Sci.*, 2015, **8**, 540–545.
57 H. Kim, R. A. Shakoor, C. Park, S. Y. Lim, J.-S. Kim, Y. N. Jo, W. Cho, K. Miyasaka, R. Kahraman, Y. Jung and J. W. Choi, *Adv. Funct. Mater.*, 2013, **23**, 1147–1155.
58 H. Kim, I. Park, D.-H. Seo, S. Lee, S.-W. Kim, W. J. Kwon, Y.-U. Park, C. S. Kim, S. Jeon and K. Kang, *J. Am. Chem. Soc.*, 2012, **134**, 10369–10372.
59 I. Hasa, J. Hassoun, Y.-K. Sun and B. Scrosati, *ChemPhysChem*, 2014, **15**, 2152–2155.
60 J. wang and X. Sun, *Energy Environ. Sci.*, 2015, **8**, 1110–1138.
61 A. Whiteside, C. A. J. Fisher, S. C. Parker and M. Saiful Islam, *Phys. Chem. Chem. Phys.*, 2014, **16**, 21788–21794.
62 J. Lu, S. C. Chung, S.-I. Nishimura and A. Yamada, *Chem. Mater.*, 2013, **25**, 4557–4565.
63 M. Galceran, D. Saurel, B. Acebedo, V. V. Roddatis, E. Martin, T. Rojo and M. Casas-Cabanas, *Phys. Chem. Chem. Phys.*, 2014, **16**, 8837–8842.
64 S.-M. Oh, S.-T. Myung, J. Hassoun, B. Scrosati and Y.-K. Sun, *Electrochem. Commun.*, 2012, **22**, 149–152.
65 F. Boucher, J. Gaubicher, M. Cuisinier, D. Guyomard and P. Moreau, *J. Am. Chem. Soc.*, 2014, **136**, 9144–9157.
66 M. Vujković and S. Mentus, *J. Power Sources*, 2014, **247**, 184–188.
67 C. Li, X. Miao, W. Chu, P. Wu and D. G. Tong, *J. Mater. Chem. A*, 2015, **3**, 8265–8271.
68 M. Pasta, C. D. Wessells, N. Liu, J. Nelson, M. T. McDowell, R. A. Huggins, M. F. Toney and Y. Cui, *Nat. Commun.*, 2014, **5**, 3007.
69 J.-Y. Luo, W.-J. Cui, P. He and Y.-Y. Xia, *Nat. Chem.*, 2010, **2**, 760–765.
70 X.-Y. Wu, M.-Y. Sun, Y.-F. Shen, J.-F. Qian, Y.-L. Cao, X.-P. Ai and H.-X. Yang, *ChemSusChem*, 2014, **7**, 407–411.
71 H. Kim, J. Hong, K.-Y. Park, H. Kim, S.-W. Kim and K. Kang, *Chem. Rev.*, 2014, **114**, 11788–11827.

72 J. Yun, J. Pfisterer and A. S. Bandarenka, *Energy Environ. Sci.*, 2016, DOI: 10.1039/C5EE03197D.
73 L. Suo, O. Borodin, T. Gao, M. Olguin, J. Ho, X. Fan, C. Luo, C. Wang and K. Xu, *Science*, 2015, **350**, 938–943.
74 A. K. Padhi, K. S. Nanjundaswamy and J. B. Goodenough, *J. Electrochem. Soc.*, 1997, **144**, 1188–1194.
75 S. W. Oh, S.-T. Myung, S.-M. Oh, K. H. Oh, K. Amine, B. Scrosati and Y.-K. Sun, *Adv. Mater.*, 2010, **22**, 4842–4845.
76 Y. J. He, J. F. Peng, W. Chu, Y. Z. Li and D. G. Tong, *J. Mater. Chem. A*, 2014, **2**, 1721–1731.
77 Y. Kim, *Phys. Chem. Chem. Phys.*, 2013, **15**, 6400–6405.
78 M. Holzapfel, A. Würsig, W. Scheifele, J. Vetter and P. Novák, *J. Power Sources*, 2007, **174**, 1156–1160.
79 J. Vetter, M. Holzapfel, A. Wuersig, W. Scheifele, J. Ufheil and P. Novák, *J. Power Sources*, 2006, **159**, 277–281.
80 J. Zheng, Y. Hou, Y. Duan, X. Song, Y. Wei, T. Liu, J. Hu, H. Guo, Z. Zhuo, L. Liu, Z. Chang, X. Wang, D. Zherebetskyy, Y. Fang, Y. Lin, K. Xu, L.-W. Wang, Y. Wu and F. Pan, *Nano Lett.*, 2015, **15**, 6102–6109.
81 X. Bogle, R. Vazquez, S. Greenbaum, A. V. W. Cresce and K. Xu, *J. Phys. Chem. Lett.*, 2013, **4**, 1664–1668.
82 A. von Cresce and K. Xu, *Electrochem. Solid-State Lett.*, 2011, **14**, A154–A156.
83 C. C. Pye, W. Rudolph and R. A. Poirier, *J. Phys. Chem.*, 1996, **100**, 601–605.
84 J. Mähler and I. Persson, *Inorg. Chem.*, 2012, **51**, 425–438.
85 S. Yanase and T. Oi, *J. Nucl. Sci. Technol.*, 2002, **39**, 1060–1064.
86 S. Y. Fu, Y. Z. Li, W. Chu, Y. M. Yang, D. G. Tong and Q. Le Zeng, *J. Mater. Chem. A*, 2015, **3**, 16716–16727.
87 Y. Cui, A. Abouimrane, J. Lu, T. Bolin, Y. Ren, W. Weng, C. Sun, V. A. Maroni, S. M. Heald and K. Amine, *J. Am. Chem. Soc.*, 2013, **135**, 8047–8056.
88 N. Ohmer, B. Fenk, D. Samuelis, C.-C. Chen, J. Maier, M. Weigand, E. Goering and G. Schütz, *Nat. Commun.*, 2015, **6**, 6045.
89 J. Wang, Y.-C. Karen, Chen. Wiegart and J. Wang, *Nat. Commun.*, 2014, **5**, 4570.
90 Q. Liu, Z.-F. Li, Y. Liu, H. Zhang, Y. Ren, C.-J. Sun, W. Lu, Y. Zhou, L. Stanciu, E. A. Stach and J. Xie, *Nat. Commun.*, 2015, **6**, 6127.
91 J. Zhong, H. Zhang, X. Sun and S.-T. Lee, *Adv. Mater.*, 2014, **26**, 7786–7806.
92 S. Pongha, B. Seekoaon, W. Limphirat, P. Kidkhunthod, S. Srilomsak, Y.-M. Chiang and N. Meethong, *Adv. Energy Mater.*, 2015, **5**, 201500663.
93 B. Guo, X. Yu, X.-G. Sun, M. Chi, Z.-A. Qiao, J. Liu, Y.-S. Hu, X.-Q. Yang, J. B. Goodenough and S. Dai, *Energy Environ. Sci.*, 2014, **7**, 2220–2226.
94 K.-W. Nam, W.-S. Yoon, K. Zaghib, K. Yoon Chung and X.-Q. Yang, *Electrochem. Commun.*, 2009, **11**, 2023–2026.
95 A. Deb, U. Bergmann, S. P. Cramer and E. J. Cairns, *Electrochim. Acta*, 2005, **50**, 5200–5207.
96 M. Galceran, V. Roddatis, F. J. Zúñiga, J. M. Pérez-Mato, B. Acebedo, R. Arenal, I. Peral, T. Rojo and M. Casas-Cabanas, *Chem. Mater.*, 2014, **26**, 3289–3294.
97 W. Dreyer, J. Jamnik, C. Guhlke, R. Huth, J. Moskon and M. Gaberscek, *Nat. Mater.*, 2010, **9**, 448–453.
98 M. Wagemaker, W. J. H. Borghols and F. M. Mulder, *J. Am. Chem. Soc.*, 2007, **129**, 4323–4327.
99 H. Liu, F. C. Strobridge, O. J. Borkiewicz, K. M. Wiaderek, K. W. Chapman, P. J. Chupas and C. P. Grey, *Science*, 2014, **344**, 6191.